High-speed, Steady Flight with a Quadrocopter in a Confined Environment Using a Tether

Maximilian Schulz, Federico Augugliaro, Robin Ritz, and Raffaello D'Andrea

Abstract— This paper presents a method that enables high-speed, steady flight in confined spaces for tethered quadrocopters. Thanks to the centripetal force exerted by the tether, high-speed trajectories along circles at different velocities, accelerations, and orientations in space can be flown. Various circular maneuvers are experimentally demonstrated, and tangential velocities of up to 15 m/s and centripetal accelerations of more than 13 g can be achieved in steady flight. The recorded data allows to characterize the flight behavior of quadrocopters at high airspeeds: As an example, an estimate of the actual thrust produced by the motors and of the aerodynamic drag acting on the vehicle is presented. An accompanying video shows tethered quadrocopters performing high-speed maneuvers.

I. Introduction

Quadrocopters are highly agile flying machines. They are able to both precisely hover in space and perform acrobatic maneuvers, such as, among others, flying through windows [1], performing flips [2] or accurately tracking aggressive periodic trajectories [3]. At such high speeds, however, simple first-principles models that neglect, for example, aerodynamic drag or propeller efficiency, do not allow for accurate tracking performance without the use of learning and adaption techniques. As such, researchers have been motivated to study the aerodynamic properties of these vehicles. In [4], momentum theory is used to propose control schemes that account for blade flapping and thrust efficiency in different flight conditions. In [5], blade element theory is used to incorporate rotor drag in both the estimators and controllers; a similar theoretical basis is used to model different kinds of drag forces acting on the vehicle in [6]. A multitude of propellers were characterized in [7] and controllers based on the generation of aerodynamic power have been proposed [8]. Most of these works evaluate their models for relatively low velocities. For higher velocities, however, wind tunnels are often required because steady flights at high airspeeds are difficult to achieve in a confined environment.

This paper presents a method for performing high-speed, steady flight with quadrocopters in a confined space. Similar to [9], a tether is exploited to fly circular trajectories. A quadrocopter is attached to a fixed point in space via a tether, such that, when flying circles at high speeds, the tether generates the required centripetal forces. Fig. 1 shows the tethered quadrocopter performing such a high-speed maneuver. Tethered flying machines allow for fuel supply [10],

improving the robustness of autonomous helicopters [11], [12], swinging from the ceiling [13], fixed position control of an airfoil [14], or formation flights of spacecrafts [15]. Tethers are used together with quadrocopters to extend their dynamic capabilities as in [16]–[18], define novel localization approaches [19], and build tensile structures [20].

The methods presented in this work allow to achieve velocities up to 15.3 m/s and, consequently, to explore various high-airspeed related phenomena, such as air resistance and actuators efficiency. Thanks to the tether, centripetal accelerations of more than $128 \, \text{m/s}^2$ are achieved with a $0.5 \, \text{kg}$ quadrocopter, whose propellers are only able to provide $3.5 \, \text{N}$ of thrust, which would result in a maximum achievable acceleration of only $28 \, \text{m/s}^2$. The system and its components (such as sensors, actuators, or batteries) can therefore be tested under high stress conditions.

The paper is organized as follows: In Section II, the system dynamics are presented. Section III describes the trajectories flown by the vehicle. Section IV presents a suitable control strategy. Section V describes experimental results and the identification of drag-related parameters. A video showing tethered quadrocopters performing high-speed maneuvers is found in the attached multimedia submission.

II. System Modeling

The goal of this work is to fly great circles on a sphere with quadrocopters at high airspeeds. Great circles are the circles that result from the intersection of the sphere with a plane that passes through the center of the sphere. To achieve large centripetal accelerations, the vehicle is attached to a fixed point in space with a tether of constant length L_t that defines the radius of the sphere. In this section, the dynamics of the system are derived.

Fig. 1. Quadrocopter attached to a tether flying high-speed maneuvers. The tether is attached to a plain bearing mounted on a rigid support structure.
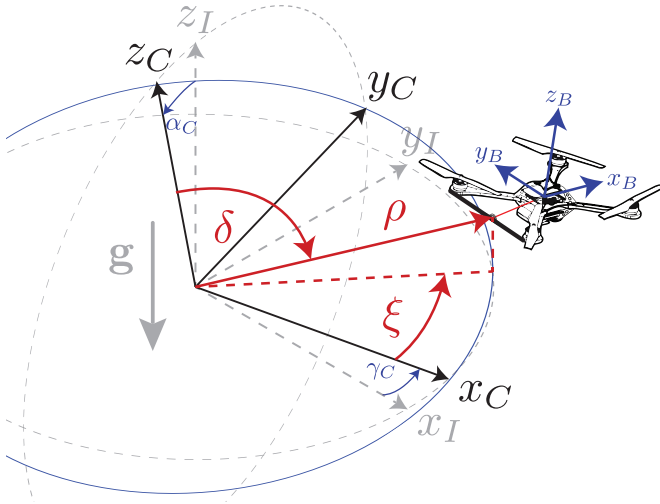
Fig. 2. Coordinate frames. The inertial frame *I* (grey) is aligned to gravity. The circle frame *C* (black) is aligned with the desired circle. The body-fixed coordinate system *B* (blue) represents the vehicle's attitude. The spherical coordinates ρ, δ, and ξ (red) indicate the position of the attachment point.

A. Great Circles

1) Coordinate Frames: A set of coordinates that facilitates the derivation of trajectories and control laws is illustrated in Fig. 2. The inertial frame *I* is defined to be a fixed frame whose *z*-axis is aligned with the gravity vector **g** and whose origin is at the fixed point of the tether. The circle frame *C* is defined by the latitude angle γ_C and the tilt angle α_C. A great circle is then defined by the intersection of the sphere and the circle frame's *xy*-plane. The rotation matrix from the circle frame *C* to the inertial frame *I* reads

$$ {}_I^C\boldsymbol{R}(\alpha_C, \gamma_C) = \boldsymbol{R}_z(\gamma_C)\boldsymbol{R}_x(\alpha_C), \tag{1} $$

where $\boldsymbol{R}_x$ and $\boldsymbol{R}_z$ denote a rotation around the *x* and *z*-axis, respectively. The body frame *B* represents the attitude of the vehicle. The rotation matrix from the body-fixed frame *B* to the circle frame *C* is given by

$$ {}_C^B\boldsymbol{R}(\phi, \theta, \psi) = \boldsymbol{R}_z(\psi)\boldsymbol{R}_y(\theta)\boldsymbol{R}_x(\phi), \tag{2} $$

where ϕ, θ, and ψ represent the roll, pitch, and yaw angles expressed in the circle frame.

2) Attachment Point Coordinates: The tether is not attached to the center of gravity (COG) of the quadrocopter, but to an outer point, referred to as the attachment point. The position of the attachment point is described in spherical coordinates by the radial distance ρ, the polar angle δ, and the azimuth angle ξ. Note that because the tether is of constant length and assumed to be taut at all times, ρ is constant.

B. Quadrocopter Model

The quadrocopter is modeled as a rigid body with six degrees of freedom. The position of its COG is given by $\boldsymbol{p}_q$, while its attitude is represented by ${}_C^B\boldsymbol{R}$. In the following equations, the variable ${}^I\boldsymbol{x}$ denotes a vector expressed in the coordinate frame *I*.

1) Control Inputs: The thrusts produced by each motor are used as control inputs. It is assumed that the thrust can be changed instantaneously.

2) Translational Dynamics: The thrust force is aligned with the vehicle's *z*-axis and the sum of the individual thrust forces T_i yields the collective thrust $T_C = \sum_{i=1}^4 T_i$. The translational dynamics of the quadrocopter are modeled as

$$ m_q{}^C\ddot{\boldsymbol{p}}_q = {}_C^B\boldsymbol{R}(\phi, \theta, \psi){}^B\boldsymbol{T}_C - m_q{}_C^I\boldsymbol{R}(\alpha_C, \gamma_C){}^I\boldsymbol{g} - {}^C\boldsymbol{f}_t - {}^C\boldsymbol{f}_a, \tag{3} $$

where $\boldsymbol{f}_t$ denotes the force produced by the tether, $\boldsymbol{f}_a$ is the aerodynamic drag, and m_q is the mass of the quadrocopter. The vectors ${}^B\boldsymbol{T}_C$ and ${}^I\boldsymbol{g}$ are given by

$$ {}^B\boldsymbol{T}_C = (0,\ 0,\ T_C), \tag{4} $$

$$ {}^I\boldsymbol{g} = (0,\ 0,\ g). \tag{5} $$

Note that for the ease of notation, vectors are expressed as *n*-tuples $\boldsymbol{x} = (x_1, x_2, \dots)$, with dimension and stacking clear from context.

3) Rotational Dynamics: The rotational dynamics are derived for the body rates $\boldsymbol{\omega}$ to be

$$ {}^B\boldsymbol{J}^B\dot{\boldsymbol{\omega}} = \sum_{i=1}^4 \left({}^B\boldsymbol{L}_i \times {}^B\boldsymbol{T}_i\right) + {}^B\boldsymbol{p}_e \times \left({}_C^B\boldsymbol{R}(\phi, \theta, \psi){}^C\boldsymbol{f}_t\right) $$
$$ - {}^B\boldsymbol{\omega} \times {}^B\boldsymbol{J}^B\boldsymbol{\omega} + {}^B\boldsymbol{T}_M, \tag{6} $$

where ${}^B\boldsymbol{J}$ is the inertia around the three body axes, $\boldsymbol{L}_i$ is the vector from the COG to the ith propeller, $\boldsymbol{T}_i$ represents each propeller thrust, and $\boldsymbol{p}_e$ is the vector from the COG to the tether attachment point, which is given by

$$ {}^B\boldsymbol{p}_e = (-L_e,\ 0,\ 0). \tag{7} $$

Additionally, ${}^B\boldsymbol{T}_M$ captures the reaction torques of the motors:

$$ {}^B\boldsymbol{T}_M = (0,\ 0,\ \kappa(T_1 - T_2 + T_3 - T_4)), \tag{8} $$

where κ is an experimentally determined constant.

C. Attachment Point Dynamics

We calculate the acceleration of the attachment point $\boldsymbol{p}_t$ using rigid body dynamics combining the translational (3) and rotational dynamics (6):

$$ {}^C\ddot{\boldsymbol{p}}_t = {}^C\ddot{\boldsymbol{p}}_q + {}_C^B\boldsymbol{R}(\phi, \theta, \psi)\left({}^B\dot{\boldsymbol{\omega}} \times {}^B\boldsymbol{p}_e + {}^B\boldsymbol{\omega} \times \left({}^B\boldsymbol{\omega} \times {}^B\boldsymbol{p}_e\right)\right). \tag{9} $$

D. Tether Modeling

There exist several ways to model a tether attached to a fixed point, all having different implications on the controller design. While in [16] a stretched tether is modeled as a linear spring to exploit its natural frequency, longitudinal dynamics of the tether, which are especially significant for long tethers, are considered in [10]. In [19], the tether is always assumed to be taut and acts as a position constraint. Because a tether material with very low density and elasticity is chosen, this is the approach used in this work, and the tether is modeled to be non-elastic and massless.

This leads to the tether force $\boldsymbol{f}_t = f_t\boldsymbol{\rho}$, whose magnitude is found using (9) and the constraint $\rho = L_t$. Note that the tether affects both the translational and rotational dynamics.

E. Aerodynamic Drag

The drag force is assumed to act only on the COG and induced torques are therefore neglected. We adopt a commonly used model that is composed of both linear and quadratic terms:

$$\boldsymbol{f}_a = -\left(\mu_1 |\boldsymbol{v}| + \mu_2 |\boldsymbol{v}|^2\right) \boldsymbol{e}_v = f_a \boldsymbol{e}_v, \tag{10}$$

where $\boldsymbol{v}$ is the velocity vector and the unit vector $\boldsymbol{e}_v$ indicates its direction. The drag coefficients μ_1 and μ_2 are found experimentally.

III. NOMINAL TRAJECTORIES

In this section, the nominal trajectories that are used for flying great circles on a sphere with radius L_r are described.

A. Great Circle Trajectory

1) Circle Definition: Circular trajectories for the attachment point are defined in the circle frame by choosing

$$\delta_d = \frac{\pi}{2},$$
$$\dot{\delta}_d = \ddot{\delta}_d = 0. \tag{11}$$

Additionally, the quadrocopter should be aligned with the direction of the tether, such that

$$\theta_d = \dot{\theta}_d = \ddot{\theta}_d = 0,$$
$$\psi_d - \xi_d = \dot{\psi}_d - \dot{\xi}_d = \ddot{\psi}_d - \ddot{\xi}_d = 0. \tag{12}$$

In the following, the azimuth angle ξ_d, the latitude angle γ_C, and the tilt angle α_C are the design parameters used to specify the desired trajectories of the vehicle. Note that γ_C does not influence the relevant dynamics, but allows to describe all possible great circles of the considered sphere.

2) Desired Body Rates: Because of the coupling of translational and rotational dynamics described in (9), the time derivative of the body rates has to be derived as well. Recall that this is due to the fact that the tether is not attached to the COG. The body rates are given by

$$^B\lfloor \boldsymbol{\omega} \times \rfloor = {}^B_I\boldsymbol{R}^T {}^B_I\dot{\boldsymbol{R}}, \tag{13}$$

where $\lfloor \boldsymbol{\omega} \times \rfloor$ denotes the skew symmetric matrix of $\boldsymbol{\omega}$ [21]. It follows that

$$^B\lfloor \dot{\boldsymbol{\omega}} \times \rfloor = {}^B_I\boldsymbol{R}^T {}^B_I\ddot{\boldsymbol{R}} + {}^B_I\dot{\boldsymbol{R}}^T {}^B_I\dot{\boldsymbol{R}}. \tag{14}$$

Inserting the desired attitude trajectory defined in (12) leads to the desired body rates and angular accelerations:

$$\boldsymbol{\omega}_d = \left(\dot{\phi}_d, \ \dot{\xi}_d \sin(\phi_d), \ \dot{\xi}_d \cos(\phi_d)\right), \tag{15}$$

$$\dot{\boldsymbol{\omega}}_d = \begin{pmatrix} \ddot{\phi}_d \\ \dot{\xi}_d \dot{\phi}_d \cos(\phi_d) + \ddot{\xi}_d \sin(\phi_d) \\ -\dot{\xi}_d \dot{\phi}_d \sin(\phi_d) + \ddot{\xi}_d \cos(\phi_d) \end{pmatrix}. \tag{16}$$

3) Desired Roll: The desired roll angle is found to be

$$\phi_d = -\operatorname{arccot}\left(\frac{g \cos \alpha_C}{g \cos \xi_d \sin \alpha_C + \frac{1}{m_q} f_a + \ddot{\xi}_d (\rho + L_e)}\right). \tag{17}$$

In order to obtain well-defined $\dot{\phi}_d$ and $\ddot{\phi}_d$, the azimuth angle acceleration $\ddot{\xi}_d$ must be twice differentiable. Note that when $\ddot{\xi}_d = 0$ and $\alpha_C = 0$, the desired roll only depends on the desired angular velocity $\dot{\xi}_d$.

4) Tether Force: The tether force corresponds to the sum of the centripetal force and the gravity vector projected along the direction of the tether, and is given by

$$f_t = m_q(\rho + L_e)\dot{\xi}_d^2 - m_q g \sin(\xi_d) \sin(\alpha_C). \tag{18}$$

For the tether to be taut at all times, i.e. $f_t > 0$, the desired angular velocity $\dot{\xi}_d$ must satisfy

$$\dot{\xi}_d > \sqrt{\frac{g}{\rho + L_e} \sin(\xi_d) \sin(\alpha_C)}. \tag{19}$$

A special case considered in this work are circular trajectories with constant angular velocities, such that $\ddot{\xi}_d = 0$. The desired angular velocity $\dot{\xi}_d$ has to be larger than the lower bounds defined by (19).

B. Speed Up and Stop Maneuvers

In order to quickly accelerate and decelerate, acceleration maneuvers for horizontal circles are defined as

$$\ddot{\xi}_d = 2a \sin^2\left(\frac{a\pi t}{v_0 - v_1}\right), \quad \text{for } t \in [0, \frac{1}{a}(v_1 - v_0)], \tag{20}$$

where a controls the desired acceleration, and v_0 and v_1 denote the initial and final velocity, respectively.

IV. CONTROL STRATEGY

This section describes the control strategy used for tracking the proposed trajectories.

A. Control Variables

The state $\boldsymbol{s}$ and control input $\boldsymbol{u}$ are defined to be

$$\boldsymbol{s} = \left(\delta, \ \xi, \ \dot{\delta}, \ \dot{\xi}, \ \phi, \ \theta, \ \chi, \ \boldsymbol{\omega}\right), \tag{21}$$
$$\boldsymbol{u} = \left(T_1, \ T_2, \ T_3, \ T_4\right), \tag{22}$$

where $\chi = \psi - \xi$ represents deviations in the yaw angle relative to the tether direction.

B. Time-Varying Linear Control

The controller tracks a desired great circle specified by the desired angular velocity profile and the tilt angle α_R. The system dynamics introduced in Section II are linearized around the desired trajectory and a finite-horizon, discrete-time LQR controller [22] with the cost function

$$J = \sum_{k=0}^{N} \left(\tilde{\boldsymbol{s}}_k^T \boldsymbol{Q} \tilde{\boldsymbol{s}}_k + \tilde{\boldsymbol{u}}_k^T \boldsymbol{R} \tilde{\boldsymbol{u}}_k\right) \tag{23}$$

is used. The vectors $\tilde{\boldsymbol{s}}_k$ and $\tilde{\boldsymbol{u}}_k$ represent the deviation from the nominal state and the nominal input at time k, respectively. To ensure a zero steady-state offset, the state error $\tilde{\boldsymbol{s}}$ is augmented with an integration state $\tilde{\boldsymbol{s}}_I$ on δ. The horizon N is chosen to be one period of the circle.

An appropriate tuning of the matrix $\boldsymbol{Q}$ has been found to be

$$\boldsymbol{Q} = \operatorname{diag}(3, \ 0.2, \ 1, \ 1, \ 1, \ 2, \ 0.5, \ 1, \ 1, \ 1, \ 0.5). \tag{24}$$

The matrix $\boldsymbol{R}$ is chosen to be the identity matrix. Low penalty on $\tilde{\chi}$ was chosen since $\tilde{\chi}$ was observed to have a self-stabilizing behavior due to the off-center mounting of the tether. Larger penalties on $\tilde{\delta}$ and $\tilde{\theta}$ were chosen because the tracking of both states is critical, especially at low velocities.
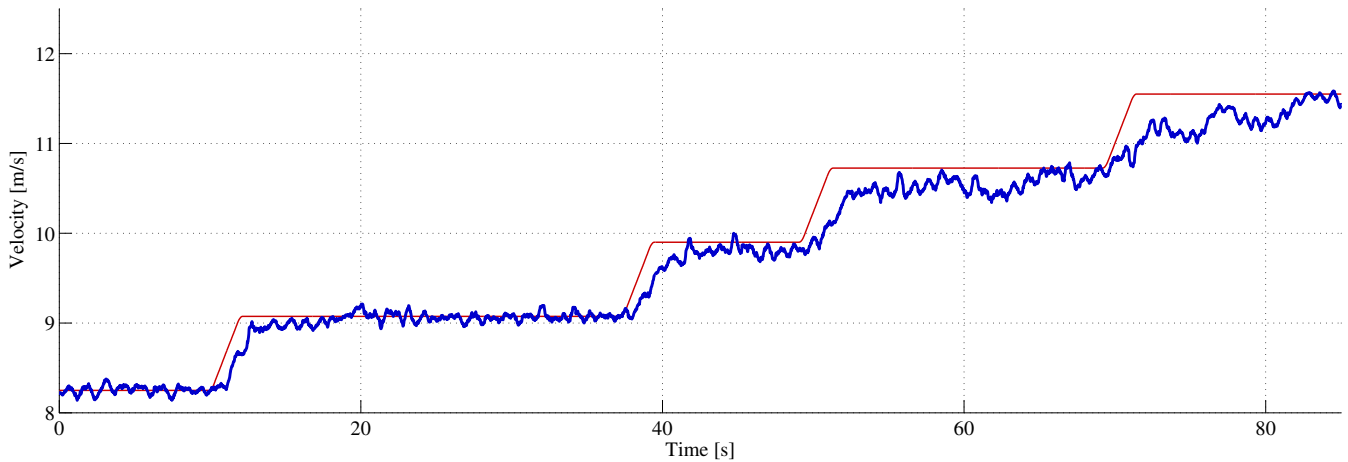
Fig. 3. Vehicle velocity. The desired velocity is shown in red, the measured velocity in blue. The controller performance decreases for high velocities, when effects such as motor efficiency decrease play a major role.

C. Gain Scheduling

As the LQR controller only guarantees performance in the vicinity of the linearization points, a gain scheduling scheme is used, that divides the non-linear task into linear sub-problems. Gain scheduling has been extensively treated in the literature and sophisticated methods exist [23]. In this work, a simple method that proved well in practice is used: a three-dimensional grid with the axes being the azimuth angle ξ, the angular velocity $\dot{\xi}$, and the tilt angle α_C is defined. The gains are then calculated for various operating points and an element-wise multivariate interpolation is then used to calculate the current gain. With this approach, we only need to calculate the points on the positive quadrant of $\dot{\xi}$ and α_C, because the full space can then be described by an appropriate coordinate transformation.

V. EXPERIMENTAL RESULTS

In this section, we introduce the experimental setup, present the performance of the proposed controller, and analyze the thrust efficiency and air resistance at high velocities. The proposed methods allow to obtain flight data at large airspeeds in a confined environment without the use of a wind tunnel.

A. Experimental Setup

The experiments are performed with small quadrocopters in the Flying Machine Arena [24], a 10x10x10 m testbed for aerial robotics research. A motion capture system provides the vehicle's position and attitude at 200 Hz. These measurements are sent to the vehicle at 50 Hz through a low-latency radio link. The quadrocopters are equipped with the Pixhawk PX4 FMU electronics [25] and industrial grade radio modules [24]. The designed estimation and control algorithms are implemented on-board and run at 1 kHz. Measurements from the on-board gyroscopes and accelerometers are used to compensate for the latency of the radio link. Furthermore, the inertial measurements are integrated in-between position and attitude updates to predict the current state.

B. Controller Performance

Circular trajectories are flown at a variety of velocities, accelerations, and tilt angles. The controller performance for constant angular velocity horizontal circles with tether radius $L_t = 1.5$ m is shown in Fig. 3. For convenience, the angular velocity is multiplied with the nominal distance from the COG to the center point. It can be seen that the desired velocity is tracked well up to a velocity of about 9 m/s. At high airspeeds modeling errors, caused for example by wrong parameters that are identified with static tests, occur that influence the tracking performance.

The deviation from the desired circle in the inertial z-axis is satisfactory: the root-mean square error in z is 0.013 m. In addition to constant velocity horizontal circles, other trajectories such as tilt angles up to 40 degrees and speed up and stop maneuvers with tangential peak accelerations up to 12.5 m/s^2 and decelerations up to 19.75 m/s^2 were tested. The controller performance for a braking maneuver is shown in Fig. 4. It can be seen how the vehicle can effectively reduce its velocity from 11.3 m/s to 1.0 m/s in under 1.5 s. This and other maneuvers are shown in the accompanying video.

C. Drag and Thrust Mapping Analysis

1) Measurement Model: The resulting steady flight enables to extract reasonable estimates of both the produced collective thrust and the aerodynamic drag acting on the quadrocopter. Position and attitude measurements provided by the motion capture system are numerically differentiated to obtain linear and angular velocities and accelerations. By using the dynamic model presented in Section II, we could solve for the unknowns T_C, f_t, and f_a. A sensitivity analysis, however, showed that these quantities are strongly affected by small errors in the tether mounting location. This is due to the fact that the force exerted by the tether is one order of magnitude larger than all other forces acting on the vehicle. We therefore adopt a simplified model, where the velocity vector v is assumed to be always tangential to the circle.

Its magnitude $|\boldsymbol{v}|$ and the corresponding time derivative $a_v = \frac{\delta}{\delta t}|\boldsymbol{v}|$ are assumed to be the vehicle's velocity and acceleration on the circle. All out-of-plane velocities and accelerations are assumed to be zero. These assumptions are motivated by the good tracking performance obtained during the experiments and illustrated in the previous section. The estimated collective thrust $\widehat{T}_C$ and drag force $\widehat{f}_a$ are calculated as

$$\widehat{T}_C = -\frac{m_q}{\cos\phi\cos\theta}\boldsymbol{g}\cdot\boldsymbol{z}_C, \tag{25}$$

$$\widehat{f}_a = \widehat{\boldsymbol{T}}_C\cdot\boldsymbol{e}_v + m_q\boldsymbol{g}\cdot\boldsymbol{e}_v - m_q a_v, \tag{26}$$

where $\boldsymbol{e}_v = \frac{\boldsymbol{v}}{|\boldsymbol{v}|}$ is the direction of the velocity and $\boldsymbol{z}_C$ is the z-axis of the circle frame. The vector $\widehat{\boldsymbol{T}}_C$ is given by

$$\widehat{\boldsymbol{T}}_C = \widehat{T}_C\boldsymbol{z}_B, \tag{27}$$

where $\boldsymbol{z}_B$ is the z-axis of the body frame.

2) Thrust Efficiency: We define a measure for the thrust efficiency as

$$\eta_f = \frac{\widehat{T}_C}{\sum_{i=1}^{4} T_{u,i}}, \tag{28}$$

where $T_{u,i}$ is the commanded thrust of motor i. The commanded thrust is based on the motor response identified from static tests. The top part of Fig. 5 shows that these static tests do not generalize to high velocities, as also noticed by e.g. [4].

This behaviour also seems to agree with the model suggested by [4], that relates the actual produced thrust T to the
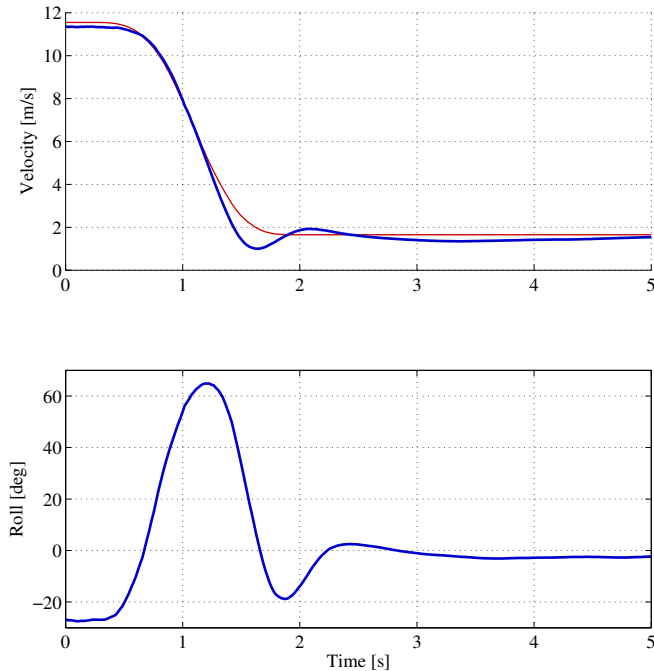

Fig. 4. Vehicle braking rapidly with a peak tangential deceleration of $17.5\,\text{m/s}^2$. The top plot shows the velocity tracking performance with the desired velocity shown in red and the measured one in blue. The bottom plot shows the corresponding roll angle.
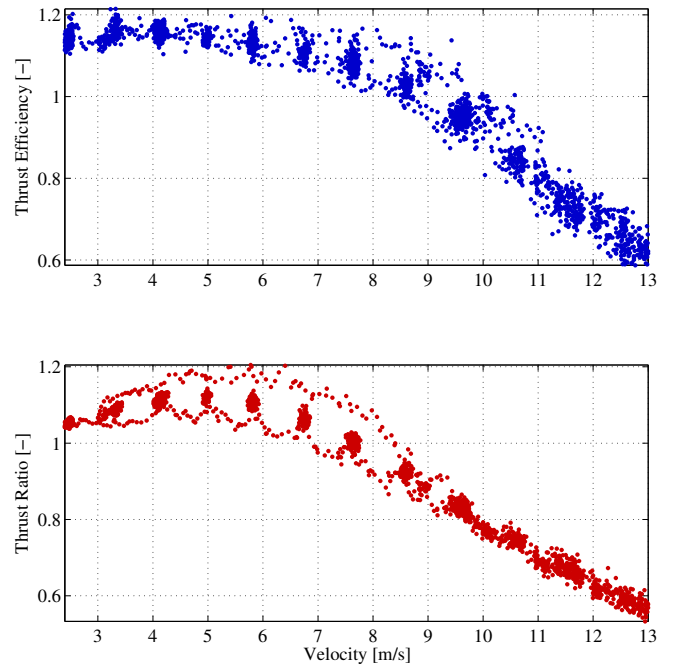

Fig. 5. The top plot shows the produced thrust divided by the commanded thrust for different airspeeds. The bottom plot shows the evaluation of (29) for our flight data.

thrust obtained at hover conditions T_h for the same power input:

$$\frac{T}{T_h} = \frac{v_h}{v_i - v_\infty\sin\beta}, \tag{29}$$

where v_i and v_h are the induced vertical velocities through the rotors for translational flight and hover conditions, respectively, and are derived according to [4]. For the purpose of this analysis, the free stream flow v_∞ is assumed to be the flight velocity and β is defined as the angle between the rotor plane and the free stream flow, where we neglect effects such as blade flapping. The resulting thrust ratio for our flight data is plotted in the bottom part of Fig. 5.

3) Drag Identification: With the recorded data, the air resistance for high velocities can be estimated as well. Fig. 6 shows the estimated drag $\hat{f}_a$ for different airspeeds. The drag model (10) is fitted to the data resulting in the drag coefficients $\mu_1 = 0.172$ and $\mu_2 = 0.0025$. The recorded data could allow to evaluate other drag models at high airspeeds.

D. Control of Multiple Quadrocopters

Two vehicles performing different circular trajectories are shown in the accompanying video. This could allow to characterize other effects, such as the flight behaviour of vehicles flying in each others wake.

VI. CONCLUSIONS

In this paper, a method for flying high-speed, high-acceleration trajectories in confined spaces with a tethered quadrocopter was presented. Thanks to the suggested strategies, the actual thrust produced by the motors and
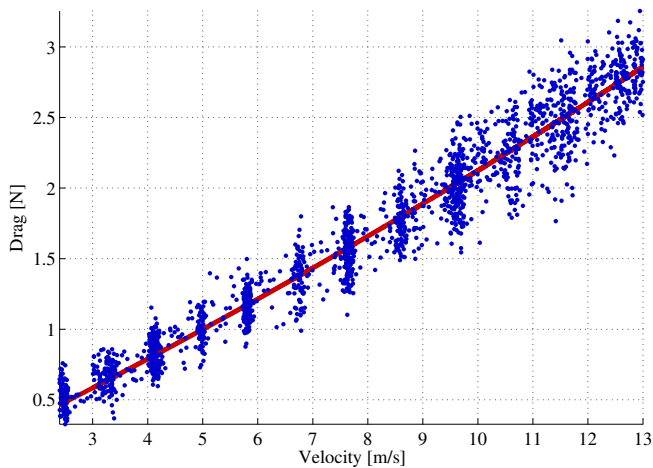
Fig. 6. The estimated aerodynamic drag is plotted in blue for different airspeeds. The red line depicts the fitted second order model (10).

the aerodynamic drag acting on the vehicle at such high airspeeds were estimated.

The proposed setup enables to characterize the flight behaviour of quadrocopters at high velocities and to stress test the system's components, such as actuators, sensors, and batteries. Such a testbed could be used to characterize aerodynamic effects in more detail and to analyze other drag models from the literature, including for example information about the propeller speeds or the vehicle's attitude. Furthermore, dynamic maneuvers at very high speed could be developed: For instance, emergency braking maneuvers for quadrocopters could be tested and optimized in a safe environment. A drawback of the proposed setup is the need for precise and accurate position and attitude information from the motion capture system. Furthermore, the vehicle's own wake could negatively affect some of the measurements. Research in this direction could be performed by flying multiple vehicles at the same time as demonstrated in the attached video.

ACKNOWLEDGMENT

REFERENCES

[1] D. Mellinger, N. Michael, and V. Kumar, "Trajectory generation and control for precise aggressive maneuvers with quadrotors," *The International Journal of Robotics Research*, pp. 664–674, 2012.

[2] S. Lupashin and R. D'Andrea, "Adaptive open-loop aerobatic maneuvers for quadrocopters," in *International Federation of Automatic Control (IFAC) World Congress*, vol. 18, 2011, pp. 2600–2606.

[3] M. Hehn and R. D'Andrea, "An iterative learning scheme for high performance, periodic quadrocopter trajectories," in *European Control Conference (ECC)*. IEEE, 2013, pp. 1799–1804.

[4] H. Huang, G. M. Hoffmann, S. L. Waslander, and C. J. Tomlin, "Aerodynamics and control of autonomous quadrotor helicopters in aggressive maneuvering," in *International Conference on Robotics and Automation (ICRA)*. IEEE, 2009, pp. 3277–3282.

[5] P. Martin and E. Salaun, "The true role of accelerometer feedback in quadrotor control," *International Conference on Robotics and Automation (ICRA)*, pp. 1623–1629, 2010.

[6] M. Bangura and R. Mahony, "Nonlinear dynamic modeling for high performance control of a quadrotor," in *Australasian conference on robotics and automation*, 2012, pp. 1–10.

[7] J. B. Brandt and M. S. Selig, "Propeller performance data at low reynolds numbers," in *49th AIAA Aerospace Sciences Meeting*, 2011, pp. 2011–1255.

[8] M. Bangura, H. Lim, H. J. Kim, and R. Mahony, "Aerodynamic power control for multirotor aerial vehicles," in *International Conference on Robotics and Automation (ICRA)*. IEEE, 2014, pp. 529–536.

[9] S. Gros, H. Ahmad, K. Geebelen, J. Swevers, and M. Diehl, "In-flight estimation of the aerodynamic roll damping and trim angle for a tethered aircraft based on multiple-shooting," in *Proceedings of the 16th IFAC Symposium on System Identification*, 2012, pp. 1407–1412.

[10] G. Schmidt and R. Swik, "Automatic hover control of an unmanned tethered rotorplatform," *Automatica*, vol. 10, no. 4, pp. 393–403, 1974.

[11] S.-R. Oh, K. Pathak, S. K. Agrawal, H. R. Pota, and M. Garratt, "Approaches for a tether-guided landing of an autonomous helicopter," *Transactions on Robotics*, vol. 22, no. 3, pp. 536–544, 2006.

[12] L. A. Sandino, M. Bejar, K. Kondak, and A. Ollero, "On the use of tethered configurations for augmenting hovering stability in small-size autonomous helicopters," *Journal of Intelligent and Robotic Systems*, vol. 70, no. 1-4, pp. 509–525, 2013.

[13] P. J. McKerrow and D. Ratner, "The design of a tethered aerial robot," in *International Conference on Robotics and Automation (ICRA)*. IEEE, 2007, pp. 355–360.

[14] S. Eeckhout, M. Nicotra, R. Naldi, and E. Garone, "Nonlinear control of an actuated tethered airfoil," in *Mediterranean Conference of Control and Automation (MED)*. IEEE, 2014, pp. 1412–1417.

[15] S.-J. Chung, "Nonlinear control and synchronization of multiple lagrangian systems with application to tethered formation flight spacecraft," Ph.D. dissertation, Massachusetts Institute of Technology, 2007.

[16] R. Ritz, M. Muller, M. Hehn, and R. D'Andrea, "Cooperative quadrocopter ball throwing and catching," in *International Conference on Intelligent Robots and Systems (IROS)*. IEEE, 2012, pp. 4972–4978.

[17] "Tethered flight in high-wind environments." [Online]. Available: http://acl.mit.edu/projects/tetheredFlight.html

[18] M. M. Nicotra, R. Naldi, E. Garone, and A. M. Studiorum, "Taut cable control of a tethered uav," in *International Federation of Automatic Control (IFAC) World Congress*, 2014, pp. 3190–3195.

[19] S. Lupashin and R. D'Andrea, "Stabilization of a flying vehicle on a taut tether using inertial sensing," in *International Conference on Intelligent Robots and Systems (IROS)*. IEEE, 2013, pp. 2432–2438.

[20] F. Augugliaro, A. Mirjan, F. Gramazio, M. Kohler, and R. D'Andrea, "Building tensile structures with flying machines," in *International Conference on Intelligent Robots and Systems (IROS)*. IEEE, 2013, pp. 3487–3492.

[21] P. C. Hughes, *Spacecraft Attitude Dynamics*. Courier Corporation, 2012.

[22] D. P. Bertsekas, *Dynamic Programming and Optimal Control*. Athena Scientific, 2005, vol. 1, no. 3.

[23] D. J. Leith and W. E. Leithead, "Survey of gain-scheduling analysis and design," *International Journal of Control*, vol. 73, no. 11, pp. 1001–1025, 2000.

[24] S. Lupashin, M. Hehn, M. W. Mueller, A. P. Schoellig, M. Sherback, and R. D'Andrea, "A platform for aerial robotics research and demonstration: The flying machine arena," *Mechatronics*, vol. 24, no. 1, pp. 41–54, 2014.

[25] L. Meier, P. Tanskanen, F. Fraundorfer, and M. Pollefeys, "Pixhawk: A system for autonomous flight using onboard computer vision," in *International Conference on Robotics and Automation (ICRA)*. IEEE, 2011, pp. 2992–2997.

[26] "Flying machine arena." [Online]. Available: http://flyingmachinearena.org/